

Elastic, Inelastic, and Path Length Fluctuations in Jet Tomography

Simon Wicks,¹ William Horowitz,¹ Magdalena Djordjevic,^{1,2} and Miklos Gyulassy¹

¹*Department of Physics, Columbia University, 538 West 120-th Street, New York, NY 10027*

²*Department of Physics, The Ohio State University,
191 West Woodruff Avenue, Columbus, OH 43210*

(Dated: February 7, 2008)

Jet quenching theory using perturbative QCD is extended to include (1) elastic as well as (2) inelastic parton energy losses and (3) jet path length fluctuations. The extended theory is applied to non-photon single electron production in central Au+Au collisions at $\sqrt{s} = 200$ AGeV. The three effects combine to significantly reduce the discrepancy between theory and current data without violating the global entropy bounds from multiplicity and elliptic flow data. We also check for consistency with the pion suppression data out to 20 GeV. Fluctuations of the jet path lengths in realistic geometry and the difference between the widths of fluctuations of elastic and inelastic energy loss are essential to take into account.

PACS numbers: 12.38.Mh; 24.85.+p; 25.75.-q

Light quark and gluon jet quenching observed via π, η suppression [1] in Cu+Cu and Au+Au collisions at $\sqrt{s} = 62 - 200$ AGeV at the Relativistic Heavy Ion Collider (RHIC) has been remarkably consistent thus far with predictions [2]-[5]. However, recent non-photon single electron data [6, 7, 8, 9, 10] (which present an indirect probe of heavy quark energy loss) have significantly challenged the underlying assumptions of the jet tomography theory (see [11]). A much larger suppression of electrons than predicted was observed in the $p_T \sim 4-8$ GeV region (see Fig. 1). These data falsify the assumption that heavy quark quenching is dominated by radiative energy loss when the bulk QCD matter parton density is constrained by the observed $dN/dy \approx 1000$ rapidity density of produced hadrons.

The observed “perfect fluidity” [12, 13] of the sQGP at long wavelengths ($p_T < 2$ GeV) provides direct evidence for highly nonperturbative bulk dynamics [14, 15]. Due to asymptotic freedom, a breakdown of perfect fluidity and nonperturbative effects are expected at p_T several times greater than the mean thermal energy, $3T \sim 1 - 2$ GeV. Prior to these electron data, pQCD based jet quenching theory provided increasingly reliable predictions above $p_T > 5 - 7$ GeV [12, 16] for the nuclear modification of light parton jets [2]-[5]. However, the non-photon single electron data however raise the question of whether the novel nonperturbative physics of the strongly interacting Quark Gluon Plasma (sQGP) [14] produced at RHIC could persist down to much smaller wavelengths than previously expected. This question is also of pragmatic importance because high p_T jets can be utilized as calibrated “external” tomographic probes of the bulk sQGP matter only if their dynamics can be predicted reliably.

The upper band of Fig. 1 shows that the predictions from [11] considerably underestimate the electron nuclear modification of data even out to $p_T \sim 8$ GeV. This discrepancy points to one or more of (1) missing perturbative QCD physics, (2) incomplete understanding of the initial heavy quark production and/or (3) novel non-

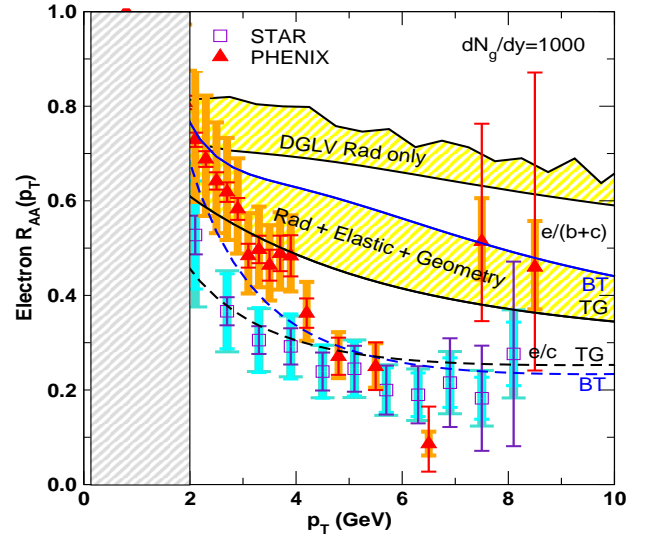


FIG. 1: The suppression factor, $R_{AA}(p_T)$, of non-photon single electron production from decay of quenched heavy quark ($c+b$) jets is compared to PHENIX [10] and STAR [9] data in central Au+Au reactions at 200 AGeV. Shaded bars indicate systematic errors, while thin error lines indicate statistical ones. All calculations assume initial $dN_g/dy = 1000$. The upper yellow band from [11] takes into account radiative energy loss only, using a fixed $L = 6$ fm; the lower yellow band is our new prediction, including both elastic and inelastic energy losses as well as jet path length fluctuations. The bands provide a rough estimate of uncertainties from the leading log approximation for elastic energy loss. The dashed curves illustrate the lower extreme of the uncertainty from production, by showing the electron suppression after both inelastic and elastic energy loss with bottom quark jets neglected.

perturbative mechanisms affecting partonic physics out to $p_T > 10$ GeV. We note that $p_T \sim 8$ GeV (single non-photon single electron) electrons originate in our calculations from the fragmentation and decay of both charm and bottom quarks with transverse momenta $p_T \sim 12 \pm 4$ GeV (see

Fig. 5 in [11]).

Possibility (3) is of course the most radical and would imply the persistence of non-perturbative physics in the sQGP down to extremely short wavelengths. Processes can be postulated to improve the fit to the data [17], but at the price of losing theoretical control of the tomographic information from jet quenching data. DGVW [11] showed that by arbitrarily increasing the initial sQGP densities to unphysical $dN_g/dy \gtrsim 4000$, the non-photonic electrons from heavy quarks can be artificially suppressed to $R_{AA} \sim 0.5 \pm 0.1$. Thus, to approach the electron data, conventional radiative energy loss requires either a violation of bulk entropy bounds or nonperturbatively large α_s extrapolations of the theory. Even by ignoring the bottom contribution, Ref. [18] found that a similarly excessive transport coefficient [20], $\hat{q}_{eff} \sim 14 \text{ GeV}^2/\text{fm}$, was necessary to approach the level of suppression of electrons in the data.

Bottom quark jets are very weakly quenched by radiative energy loss. Using the FONLL production cross-sections, their contribution significantly reduces the single electron suppression [11] compared to that of the charm jets alone. The ratio R_{AA} is not sensitive to the scaling of all cross-sections by a constant. However, it is sensitive to any uncertainty in the relative contribution of charm and bottom jets to the electrons [19]. Recent data from STAR on electrons from p+p collisions [7] may indicate an even larger uncertainty in the production than expected from FONLL. However, PHENIX p+p to electron data are compatible with the upper limit of FONLL predictions [21, 22], similar to the comparison between FONLL and Tevatron data.

The discrepancy between the ‘DGLV Rad only’ predictions and the data in Fig. 1 and recent work [23, 24, 25] motivated us to revisit the assumption that pQCD elastic energy loss [26] is negligible compared to radiative. In earlier studies, the elastic energy loss [26, 27, 28, 29, 30, 31] was found to be $dE^{el}/dx \sim 0.3 - 0.5 \text{ GeV}/\text{fm}$, which was erroneously considered to be small compared to the several GeV/fm expected from radiative energy loss. The apparent weakness of conventional pQCD collisional energy loss mechanisms was also supported by parton transport theory results [32]-[33], which showed that the typical thermal pQCD elastic cross section, $\sigma_{el} \sim 3\text{mb}$, is too small to explain the differential elliptic flow at high $p_T > 2 \text{ GeV}$ and also underestimates the high p_T quenching of pions.

In contrast, Mustafa [23] found that radiative and elastic average energy losses for heavy quarks were in fact comparable over a very wide kinematic range accessible at RHIC. In Fig. 2, we confirm Mustafa’s finding and extend it to the light quark sector as well. The fractional energy loss, $\Delta E/E$, from DGLV radiative for u, c, b quarks (solid curves; see also App. IB) is compared to TG [27] and BT [28] estimates of elastic (dashed curves; see also App. IA). For light quarks, the elastic energy loss decreases more rapidly with energy than radiative energy loss, but even at 20 GeV the elastic is only 50%

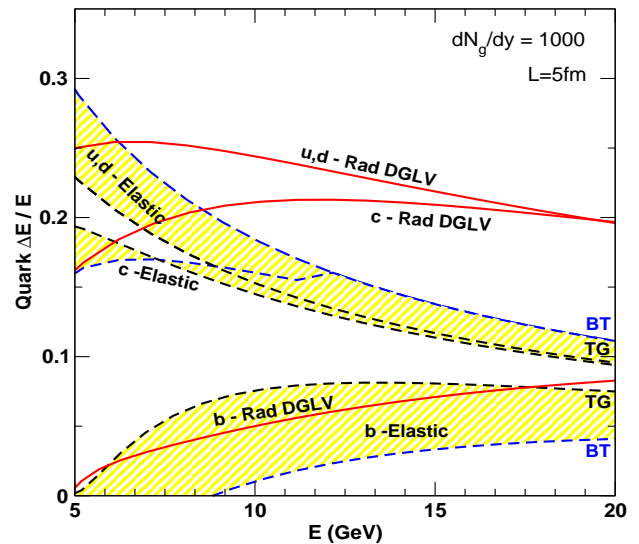


FIG. 2: Average $\Delta E/E$ for u, c, b quarks as a function of E . A Bjorken expanding QGP with path length $L = 5 \text{ fm}$ and initial density fixed by $dN_g/dy = 1000$ is assumed. The curves are computed with the coupling $\alpha_s = 0.3$ held fixed. For Debye mass $\mu_D \propto (dN_g/dy)^{1/3}$, the gluon mass is $\mu_D/\sqrt{2}$, the light quark mass is $\mu_D/2$, the charm mass is 1.2 GeV, and the bottom mass is 4.75 GeV. Radiative DGLV first order energy loss is compared to elastic parton energy loss (in TG or BT approximations). The yellow bands provide an indication of theoretical uncertainties in the leading log approximation to the elastic energy loss.

smaller than the radiative.

From Fig. 2 we see that for $E > 10 \text{ GeV}$ light and charm quark jets have elastic energy losses smaller but of the same order of magnitude as the inelastic losses. But due to the large mass effect [34]-[39],[18], both radiative and elastic energy losses remain significantly smaller for bottom quarks than for light and charm quarks, but the elastic energy loss can now be greater than inelastic up to $\sim 15 \text{ GeV}$. We present both TG and BT as a measure of the theoretical uncertainties of the Coulomb log (see App IC for benchmark numerical examples). These are largest for the heaviest b quark. As they are not ultra-relativistic, the leading log approximation [27, 28] breaks down in the kinematic range accessible at RHIC. More rigorous computations of elastic energy loss [50] and numerical covariant transport techniques [32] can be used to reduce the theoretical uncertainties in the elastic energy loss effects.

Theoretical Framework.

The quenched spectra of partons, hadrons, and leptons are calculated as in [11] from the generic pQCD convolution

$$\frac{E d^3 \sigma(e)}{dp^3} = \frac{E_i d^3 \sigma(Q)}{dp_i^3} \otimes P(E_i \rightarrow E_f) \otimes D(Q \rightarrow H_Q) \otimes f(H_Q \rightarrow e), \quad (1)$$

where Q denotes quarks and gluons. For charm and bottom, the initial quark spectrum, $E d^3 \sigma(Q)/dp^3$, is com-

puted at next-to-leading order using the code from [21, 22]; for gluons and light quarks, the initial distributions are computed at leading order as in [5]. $P(E_i \rightarrow E_f)$ is the energy loss probability, $D(Q \rightarrow H_Q)$ is the fragmentation function of quark Q to hadron H_Q , and $f(H_Q \rightarrow e)$ is the decay function of hadron H_Q into the observed single electron. We use the same mass and factorization scales as in [40] and employ the CTEQ5M parton densities [42] with no intrinsic k_T . As in [40] we neglect shadowing of the nuclear parton distribution in this application.

We assume that the final quenched energy, E_f , is large enough that the Eikonal approximation can be employed. We also assume that in Au+Au collisions, the jet fragmentation function into hadrons is the same as in e^+e^- collisions. This is expected to be valid in the deconfined medium case, where hadronization of $Q \rightarrow H_Q$ cannot occur until the quark emerges from the sQGP.

The main difference between our previous calculation [11] and the present one is the inclusion of two new physics components in the energy loss probability $P(E_i \rightarrow E_f)$. First, $P(E_i \rightarrow E_f)$ is generalized to include for the first time both elastic and inelastic energy loss and their fluctuations. We note that Vitev [43] was the first to generalize the GLV formalism to include *initial state* elastic energy loss effects in d+Au. In this work, Eq. (2) extends the formalism to include *final state* elastic energy loss effects in $A + A$.

The second major change relative to our previous applications is that we now take into account geometric path length fluctuations as follows:

$$P(E_i \rightarrow E_f - \Delta_{rad} - \Delta_{el}) = \int \frac{d\phi}{2\pi} \int \frac{d^2\vec{x}_\perp}{N_{bin}(b)} T_{AA}(\vec{x}_\perp, \vec{b}) \otimes P_{rad}(\Delta_{rad}; L(\vec{x}_\perp, \phi)) \otimes P_{el}(\Delta_{el}; L(\vec{x}_\perp, \phi)). \quad (2)$$

Here

$$L(\vec{x}_\perp, \phi) = \int d\tau \rho_p(\vec{x}_\perp + \tau \hat{n}(\phi)) / \langle \rho_p \rangle \quad (3)$$

is the locally determined effective path length of the jet given its initial production point \vec{x}_\perp and its initial azimuthal direction ϕ relative to the impact parameter plane (x, y) . The geometric path averaging used here is similar to that used in [44] and by Eskola et al. [45]. However, the inclusion of elastic energy losses together with path fluctuations in more realistic geometries was not considered before.

We consider a diffuse Woods-Saxon nuclear density profile [46], which creates a participant transverse density, $\rho_p(\vec{x}_\perp)$, computed using the Glauber profiles, $T_A(\vec{x})$, with inelastic cross section $\sigma_{NN} = 42$ mb. The bulk sQGP transverse density is assumed to be proportional to this participant density, and its form is shown (for the $y = 0$ slice) in Fig. 3 by the curve labeled ρ_{QGP} . The distribution of initial hard jet production points, \vec{x}_\perp , is

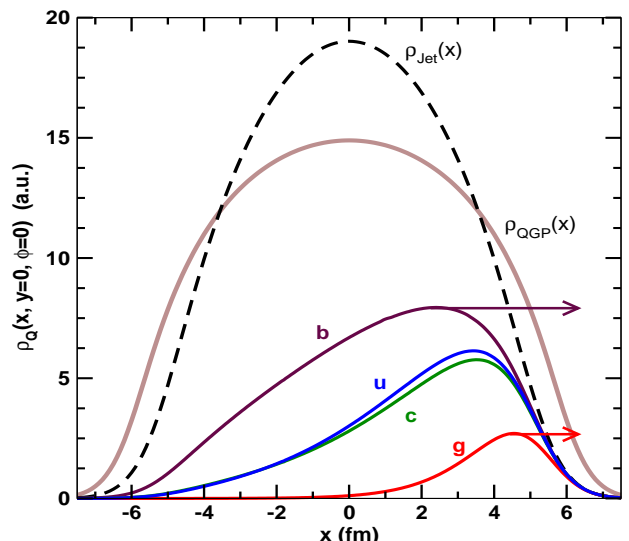


FIG. 3: Transverse coordinate $(x, 0)$ distribution of surviving $p_T = 15$ GeV, $Q = g, u, c, b$ jets moving in direction $\phi = 0$ as indicated by the arrows. Units are arbitrary for illustration. The transverse (binary collision) distribution of initial jet production points, $\rho_{jet}(x, 0)$, is shown at midrapidity for Au+Au collisions at $b = 2.1$ fm. The ratio ρ_Q/ρ_{jet} (see Eq.(8)) gives the local quenching factor including elastic and inelastic energy loss though the bulk QGP matter distributed as $\rho_{QGP}(x, 0)$.

assumed on the other hand to be proportional to the binary collision density, $T_{AA} = T_A(\vec{x} + \vec{b}/2)T_A(\vec{x} - \vec{b}/2)$. This is illustrated in Fig. 3 by the narrower curve labeled ρ_{jet} .

The combination of fluctuating DGLV radiative [35] with the new elastic energy losses and fluctuating path lengths (via the extra $d^2\vec{x}_\perp d\phi$ integrations) adds a high computational cost to the extended theory specified by Eqs. (1,2). In this first study with the extended theory, we explore the relative order of magnitude of the competing effects by combining two simpler approaches.

In approach I, we parameterize the heavy quark pQCD spectra by a simpler power law, $Ed^3\sigma_Q/d^3k \propto 1/p_T^{n+2}$, with a slowly varying logarithmic index $n \equiv n(p_T)$. For the pure power law case, the partonic modification factor, $R_Q = d\sigma_Q^{final}/d\sigma_Q^{initial}$, (prior to fragmentation) is greatly simplified. This enables us to perform the path length fluctuations numerically via

$$R_Q^I = \int \frac{d\phi}{2\pi} \int \frac{d^2\vec{x}_\perp}{N_{bin}(b)} T_{AA}(\vec{x}_\perp, \vec{b}) \int d\epsilon (1 - \epsilon)^n P_Q^I(\epsilon; L(\vec{x}_\perp, \phi)), \quad (4)$$

where

$$P_Q^I(\epsilon; L) = \int dx P_{Q,rad}(x; L) P_{Q,el}(\epsilon - x; L). \quad (5)$$

Both the mean and width of those fractional energy losses depend on the local path length. (See App ID for numer-

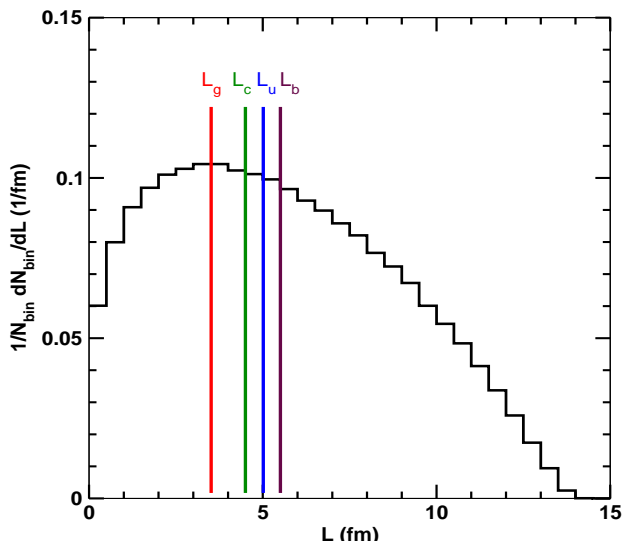


FIG. 4: Distribution of path lengths (given by Eq. (3)) traversed by hard scatterers in 0-5% most central collisions; the lengths, $L(\vec{x}_\perp, \phi)$, are weighted by the probability of production and averaged over azimuth. An equivalent formulation of Eq. (4) is $R_Q^I = \int dL 1/N_{bin} dN_{bin}/dL \int d\epsilon (1 - \epsilon)^n P_Q^I(\epsilon; L)$. Since the distribution $1/N_{bin} dN_{bin}/dL$ is a purely geometric quantity, it is the same for all jet varieties. Also displayed are the single, representative pathlengths, L_Q , used as input in approach II. Note the hierarchy of scales with glue requiring the shortest, then charm, light quarks, and bottom the longest effective pathlength.

ical illustrations of Eq.(5) for a fixed $L = 5$ fm light quark case.)

We emphasize, however, that no externally specified *a priori* path length, L , appears in Eq. (4); the path lengths are allowed to explore the whole geometry. Fig. 4 shows the broad distribution of lengths probed by hard partons in approach I.

In the second approach, we determine effective path lengths, L_Q , for each parton flavor, Q , by varying fixed L predictions $R_Q^{II}(p_T, L)$ and comparing to approach I; see Fig. 4. In approach II, $R_Q^{II}(p_T, L)$ is calculated directly from Eq. (1) with $P(E_i \rightarrow E_f)$ in Eq. (2) replaced by the fixed L approximation

$$P(E_i \rightarrow E_i - \Delta_{el} - \Delta_{rad}, L) \approx P_{rad}(\Delta_{rad}; L) \otimes P_{el}(\Delta_{el}; L). \quad (6)$$

Here, jet quenching is performed via two independent branching processes in contrast to the additive convolution in Eq. (4). For small energy losses the two approaches are similar. They differ however in the case of long path lengths when the probability of complete stopping approaches unity. In the convolution method, the probability of $\epsilon > 1$ is interpreted as complete stopping, whereas in the branching algorithm the long path length case is just highly suppressed. In both cases we take into account the small finite probability that the fractional energy loss $\epsilon \leq 0$ due to fluctuations.

To illustrate the difference in approach II, consider the case of power law initial Q distributions as in Eq. (4). In this case

$$R_Q^{II}(p_T, L_Q) \equiv \langle (1 - \epsilon_Q^r(L_Q))^n (1 - \epsilon_Q^e(L_Q))^n \rangle_{\Delta E}. \quad (7)$$

The branching implementation is seen via the product of two distinct factors in contrast to the one quenching factor in Eq. (4). For small $\langle \epsilon_Q^{r,e} \rangle$ both approaches obviously give rise to the same $R_Q = 1 - n\langle \epsilon_Q \rangle$.

Due to the high computational cost in approach I, only the TG elastic is used for the heavy quarks and only BT for light quarks. The Coulomb log uncertainties are estimated only in approach II.

In both approaches, fluctuations of the radiative energy loss due to gluon number fluctuations are computed as discussed in detail in Ref. [11, 38]. This involves using the DGLV generalization [35] of the GLV opacity expansion [3] to heavy quarks. Bjorken longitudinal expansion is taken into account by evaluating the bulk density at an average time $\tau = L/2$ [11, 38]. For elastic energy loss, the full fluctuation spectrum is approximated here by a Gaussian centered at the average energy loss with variance $\sigma_{el}^2 = 2T\langle \Delta E^{el}(p_T, L) \rangle$ [33]. In approach I the correct, numerically intensive integration through the Bjorken expanding medium provides $\Delta E^{el}(p_T, L)$. In approach II the $\tau = L/2$ approximation is again used; numerical comparisons show that for $L \sim 2 - 7$ fm this reproduces the full calculation well. Finally, we note that we use the additional numerical simplification of keeping the strong coupling constant α_s fixed at 0.3.

Numerical Results: Parton Level

In Fig. 5, we show the quenching pattern of Q from the second approach for a “typical” path length scale $L = 5$ fm, similar to that used in previous calculations [11]. The curves show $R_Q(p_T)$, prior to hadronization, for $Q = g, u, c, b$. The dashed curves show the quenching arising from only the DGLV radiative energy loss. The solid curves show the full results after including TG elastic as well as DGLV radiative energy loss. Adding elastic energy loss is seen to increase the quenching of all flavors for fixed path length. Note especially the strong nonlinear increase of the gluon suppression and the factor ~ 2 increase of the bottom suppression. The curious switch of the u and the c quenching reflects the extra valence (smaller index n_u) contribution to light quarks.

Fig. 5 emphasizes the unavoidable result of using a fixed, “typical” path length scale, L , in jet tomography: the pion and single electron quenching can never be similar. If pions were produced only by light quarks and electrons only by charm, then we would expect comparable quenching for both. However, contributions from highly quenched gluons decrease the pion R_{AA} while weakly quenched bottom quarks increase the electron R_{AA} . Therefore, in the fixed length scenario, we expect a noticeable difference between pion and single electron suppression patterns.

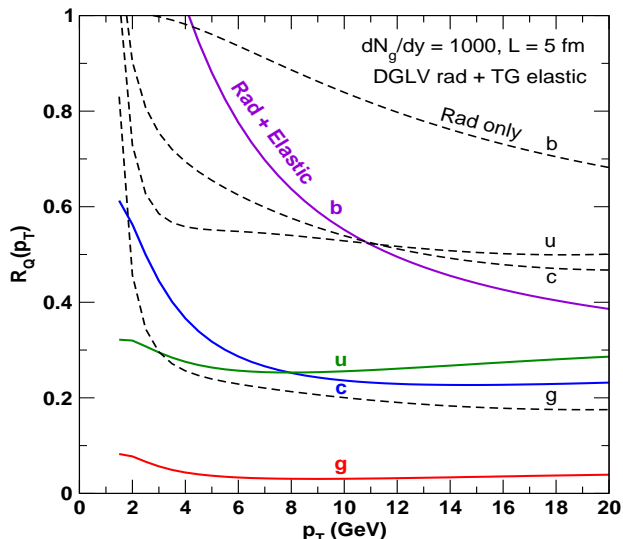


FIG. 5: Partonic nuclear modification, $R_Q^{II}(p_T)$ via Eq.(7), for g, u, c, b as a function of p_T for fixed $L=5$ fm path length and $dN_g/dy = 1000$. Dashed curves include only radiative energy loss, while solid curves include elastic energy loss as well.

The solid curves of Fig. 3 labeled by the parton flavor $Q = g, u, c, b$ show the relative transverse coordinate density of surviving jets defined by

$$\rho_Q(\vec{x}, \phi) \equiv \rho_{\text{Jet}}(\vec{x}) \int d\epsilon (1 - \epsilon)^n P_Q^I(\epsilon; L(\vec{x}, \phi)). \quad (8)$$

ρ_Q is given by the initial transverse \vec{x} production distribution times the quenching factor from that position in direction ϕ with final momentum p_T . The case shown is for a $p_T = 15$ GeV jet produced initially at $(x, 0)$ and moving in the direction $\phi = 0$ along the positive x axis. The quenching is determined by the participant bulk matter along its path $\rho_{\text{QGP}}(x + vt, 0, t)$, and varies with x because the local path length $L = L(x, 0, 0)$ changes according to Eq. (3).

What is most striking in Fig. 3 is the hierarchy of Q -dependent length scales. No single, representative path length can account for the distribution of all flavors. In general heavier flavors are less biased toward the surface (in direction ϕ) than lighter flavors since the energy loss decreases with the parton mass. Gluons are more surface biased than light quarks due to their color Casimir enhanced energy loss. In addition, note the surprising reversal of the u and c suppressions, also seen in Fig. 5. Fig. 2 shows that the energy loss of c is somewhat less than for u ; however, the higher p_T power index, n , of c relative to u – as predicted by pQCD and due to the valence component of u – compensates by amplifying its quenching.

However, none of the distributions can be categorized as surface emission. The characteristic widths of these distributions range from $\Delta x \approx 3 - 6$ fm. We show below that such a large dynamic range of path length fluctuations is essential for consistent reproduction of both

electron and pion data.

We turn next to Figs. 6 and 7, which show the interplay between the dynamical geometry seen in Fig. 3 and the elastic-enhanced quenching of partons. In Figs. 6 and 7 the solid green curves labeled “DGLV+TG/BT: Full Geometry” are the results using approach I based on Eq. (4). The curves labeled TG and BT are from approach II based on Eq. (7). The effective fixed L_Q in II were taken to match approximately the green curves in which full path length fluctuations are taken into account. This procedure is not exact because of the different numerical approximations involved, but the trends are well reproduced. The L_Q are determined only to ~ 0.5 fm accuracy, as this suffices for our purposes here. We show the comparison between approaches I and II for heavy quarks in Fig. 6 using $L_c = 4.5$ and $L_b = 5.5$ fm and for gluons and light quarks in Fig. 7 using $L_g = 3.5$ and $L_u = 5.0$ fm; see Fig. 4 for a visual comparison of the input length distributions used. This hierarchy of Q -dependent length scales is in accord with that expected from Fig. 3.

Note that in comparison to the fixed $L = 5$ fm case in Fig. 5, geometric fluctuations reduce gluon jet quenching in Fig. 7 by a factor ~ 2 . Nevertheless, even with path length fluctuations the gluons are still quenched by a factor of 10 when elastic energy loss is included in addition to radiative.

The amplified role of elastic energy loss is due to its

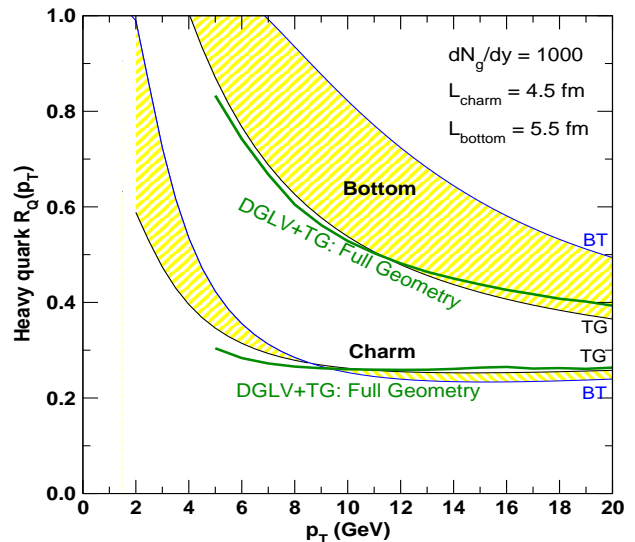


FIG. 6: Heavy quark jet quenching before fragmentation into mesons for $dN_g/dy = 1000$. Solid green curves show the results of approach I based on Eq. (4) including full geometric path length fluctuations and DGLV radiative and TG elastic energy loss for c and b quarks. Upper and lower yellow bands show predictions using approach II via Eq. (7) with effective path lengths taken as $L_c = 4.5$ and $L_b = 5.5$ fm. As previously noted in Fig. 2, the difference between TG and BT curves indicates an estimate of the magnitude of theoretical uncertainties in the elastic energy loss.

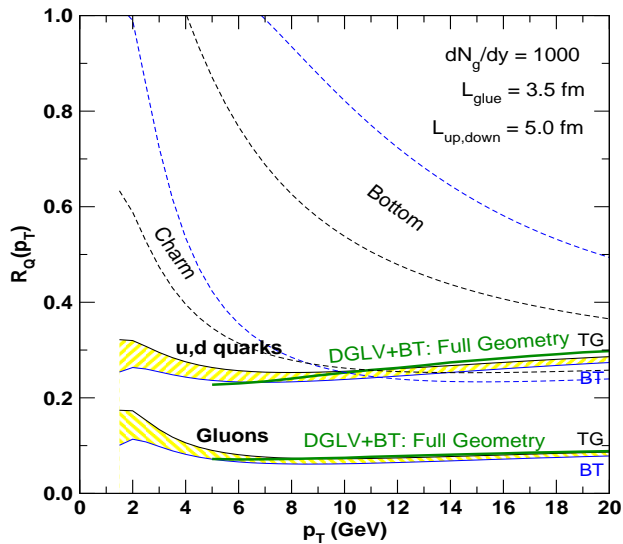


FIG. 7: As in Fig. 6 but for light u, d quarks and gluons. The yellow bands are computed in this case with effective g, u path lengths $L_g = 3.5$ and $L_u = 5.0$ fm based on Eq. (7). Note that charm and light quark quenching are similar in this p_T range.

smaller width for fluctuations relative to radiative fluctuations. Even in moderately opaque media with $L/\lambda \sim 10$, inelastic energy loss fluctuations are large because only a few, 2-3, extra gluons are radiated [4]. Thus, gluon number fluctuations, $O(1/\sqrt{N_g})$ lead to a substantial reduction in the effect of radiative energy loss. On the other hand, elastic energy loss fluctuations are controlled by collision number fluctuations, $O(\sqrt{\lambda/L})$, which are relatively small in comparison for a significant proportion of the length scales probed. Therefore, fluctuations of the elastic energy loss do not dilute the suppression of the nuclear modification factor as much as N_g fluctuations. The increase in the sensitivity of the final quenching level to the opacity is a novel and useful byproduct of including the elastic channel; see Fig. 11 in Appendix D. The inclusion of elastic energy loss significantly reduces the fragility of pure radiative quenching [45] and therefore increases the sensitivity of jet quenching to the opacity of the bulk medium [47].

Numerical Results: Pions and Electrons

We now return to Fig. 1 to discuss the consequence of including elastic energy loss of c and b quarks on the electron spectrum. The inclusion of the collisional energy loss significantly improves the comparison between theory and the single electron data. That is, the lower yellow band can reach below $R_{AA} \sim 0.5$ in spite of keeping $dN_g/dy = 1000$, consistent with measured multiplicity, and using a conservative $\alpha_s = 0.3$. A large source of the uncertainty represented by the lower yellow band is the modest but poorly determined elastic energy loss, $\Delta E/E \approx 0.0-0.1$, of bottom quarks (see Fig. 2). There is additional uncertainty from the relative contributions to electrons from charm and bottom jets. The dashed lines show an extreme version of this in which charm jets are

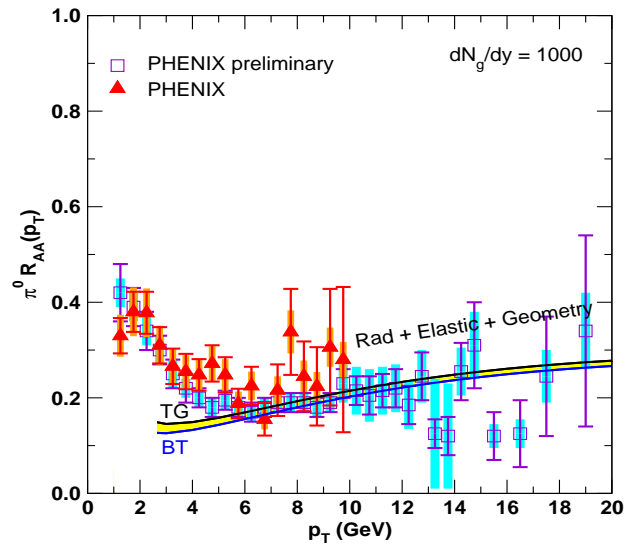


FIG. 8: The consistency of the extended jet quenching theory is tested by comparing its prediction to the nuclear modification of the π^0 spectra observed by PHENIX [1].

the only source of electrons. If the charm to bottom ratio given by FONLL calculations is accurate, the current data suggests that even the combined radiative+elastic pQCD mechanism is not sufficient to explain the single electron suppression.

As emphasized in [11], any proposed energy loss mechanisms must also be checked for consistency with the extensive pion quenching data [1], for which preliminary data now extend out to $p_T \sim 20$ GeV. This challenge is seen clearly in Fig. 5, where for fixed $L = 5$ fm, the addition of elastic energy loss would overpredict the quenching of pions. However, the simultaneous inclusion of path fluctuations leads to a decrease of the mean g and u, d path lengths that partially offsets the increased energy loss. Therefore, the combined three effects considered here makes it possible to satisfy $R_{AA}^e < 0.5 \pm 0.1$ without violating the bulk $dN_g/dy = 1000$ entropy constraint and without violating the pion quenching constraint $R_{AA}^{\pi^0} \approx 0.2 \pm 0.1$ now observed out to 20 GeV; see Fig. 8. We note that the slow rise of $R_{AA}^{\pi^0}$ with p_T in the present calculation is due in part to the neglect of initial k_T smearing that raises the low p_T region and the EMC effect that lowers the high p_T region (see [5]).

Conclusions

The elastic component of the energy loss cannot be neglected when considering pQCD jet quenching. While the results presented in this paper are encouraging, further improvements of the jet quenching theory will be required before stronger conclusions can be drawn.

From an experimental perspective, there is at present significant disagreement between measured p+p to electron baselines [7, 8]. In addition, direct measurement of D spectra will be essential to deconvolute the different bottom and charm jet quark dynamics.

On the theoretical side, more work is needed to sort out coherence and correlation effects between elastic and inelastic processes that occur in a finite time and with multiple collisions. Classical electrodynamics calculations presented in [48] suggested that radiative and elastic processes could destructively interfere over lengths far longer than previously thought. As described in [49], a proper accounting of the current shows finite size effects persist out only to the expected lengths of order the screening scale, $1/\mu_D \lesssim 1$ fm. Additionally, work on the quantum mechanical treatment of elastic energy loss in a finite medium [50, 51] also concluded that finite size effects on R_{AA} remain small except in peripheral collisions.

There are several other open problems that require further study. The inclusion of all the initial state effects from [5] will be needed to fully check the consistency of the pion predictions with the data. Only an approximate fluctuation spectrum for elastic energy loss has been included here; still needed is an examination of the effect of the full fluctuation spectrum.

The radiative and elastic energy losses depend sensitively on the coupling, $\Delta E^{rad} \propto \alpha_s^3$ and $\Delta E^{el} \propto \alpha_s^2$. Future calculations will have to relax the current fixed α_s approximation. In [52], the running of the coupling is seen to increase the magnitude of the elastic energy loss and alter the energy dependence. More complete calculations of both radiative and elastic energy losses will involve integrals that probe momentum scales that are certainly nonperturbative. Therefore it will be important to study the irreducible uncertainty associated with the different maximum α_s cutoff prescriptions commonly used.

Acknowledgments: Valuable input from Azfar Adil on parton spectra and discussions with Xin Dong, Barbara Jacak, John Harris, Peter Lévai, Denes Molnar, Thomas Ullrich, Ivan Vitev, Xin-Nian Wang, and Nu Xu are gratefully acknowledged. This work is supported by the Director, Office of Science, Office of High Energy and Nuclear Physics, Division of Nuclear Physics, of the U.S. Department of Energy under Grants No. DE-FG02-93ER40764. M. D. acknowledges support by the U.S. Department of Energy under Grants No. DE-FG02-01ER41190 during the final parts of this work.

I. APPENDIX

A. Collisional Energy Loss

The leading logarithmic expression for the elastic energy loss of a jet with color Casimir C_R in an ideal quark-gluon plasma with n_f active quark flavors and temperature, T , is given by [26]

$$\frac{dE^{el}}{dx} = C_R \pi \alpha_s^2 T^2 \left(1 + \frac{n_f}{6}\right) f(v) \log(B_c) \quad (9)$$

where the Coulomb log is controlled by the ratio B_c that involves relevant minimum and maximum momen-

tum transfers or impact parameters. For scattering in an assumed ultrarelativistic ($m = 0$) gas of partons the jet velocity dependence is

$$f(v) = \frac{1}{v^2} \left(v + \frac{1}{2}(v^2 - 1) \log\left(\frac{1+v}{1-v}\right) \right) \xrightarrow{v \rightarrow 1} 1 \quad (10)$$

Estimates for B_c differ below asymptotic ($E \gg T$) energies and are given in [26], [27], and [28] that we denote by Bj, TG, and BT respectively:

$$\begin{aligned} B_{Bj} &= (4E_p T) / (\mu^2) \\ B_{TG} &= \left(\frac{4pT}{(E_p - p + 4T)} \right) / (\mu) \\ B_{BT} &= \begin{cases} \left(2^{\frac{n_f}{6+n_f}} 0.85 E_p T \right) / \left(\frac{\mu^2}{3} \right) & E_p \gg \frac{M^2}{T} \\ \left(4^{\frac{n_f}{6+n_f}} 0.36 \frac{(E_p T)^2}{M^2} \right) / \left(\frac{\mu^2}{3} \right) & E_p \ll \frac{M^2}{T} \end{cases} \end{aligned} \quad (11)$$

with the crossover between $E_p \ll \frac{M^2}{T}$ and $E_p \gg \frac{M^2}{T}$ being taken at $E_p = \frac{2M^2}{T}$ for numerical computation.

B. DGLV Radiative Energy Loss

For completeness we also record the DGLV formula for radiative energy loss used in our calculations. We neglect finite kinematic limits on the momentum transfer q integral, and perform the finite $0 < k_\perp \leq k_{max} = 2px(1-x)$ and azimuthal $0 \leq \phi \leq 2\pi$ integrations analytically. The mean fractional radiative energy loss can be then evaluated numerically from the expression

$$\frac{\Delta E_{ind}^{(1)}}{E} = \frac{C_F \alpha_s}{\pi} \frac{L}{\lambda_g} \int_{\frac{m_g}{E_p+p}}^{1-\frac{M}{E_p+p}} dx \int_0^\infty \frac{4\mu^2 q^3 dq}{\left(\frac{4Ex}{L}\right)^2 + (q^2 + \beta^2)^2} \times (A \log B + C) \quad (12)$$

where

$$\beta^2 = m_g^2(1-x) + M^2 x^2 \quad (13)$$

$$\lambda_g^{-1} = \rho_g \sigma_{gg} + \rho_q \sigma_{qg} \quad (14)$$

$$\sigma_{gg} = \frac{9\pi\alpha_s^2}{2\mu^2} \text{ and } \sigma_{qg} = \frac{4}{9}\sigma_{gg} \quad (15)$$

We employ the asymptotic 1-loop transverse gluon mass $m_g = \mu/\sqrt{2}$. The A,B,C functions denote

$$A = \frac{2\beta^2}{f_\beta^3} (\beta^2 + q^2) \quad (16)$$

$$B = \frac{(\beta^2 + K)(\beta^2 Q_\mu^- + Q_\mu^+ Q_\mu^+ + Q_\mu^+ f_\beta)}{\beta^2(\beta^2(Q_\mu^- - K) - Q_\mu^- K + Q_\mu^+ Q_\mu^+ + f_\beta f_\mu)} \quad (17)$$

$$\begin{aligned} C &= \frac{1}{2q^2 f_\beta^2 f_\mu} [\beta^2 \mu^2 (2q^2 - \mu^2) + \beta^2 (\beta^2 - \mu^2) K \\ &\quad + Q_\mu^+ (\beta^4 - 2q^2 Q_\mu^+) + f_\mu (\beta^2 (-\beta^2 - 3q^2 + \mu^2) \\ &\quad + 2q^2 Q_\mu^+) + 3\beta^2 q^2 Q_\mu^-] \end{aligned} \quad (18)$$

E_{jet} (GeV)	Radiative $\frac{\Delta E}{E}$		Collisional $\frac{\Delta E}{E}$	
	DGLV	Bj	TG	BT
10	0.2111	0.2022	0.1594	0.1596
11	0.2126	0.1894	0.1506	0.1552
12	0.2129	0.1782	0.1430	0.1621
13	0.2123	0.1683	0.1358	0.1530
14	0.2110	0.1596	0.1294	0.1450
15	0.2093	0.1518	0.1237	0.1379

TABLE I: $\frac{\Delta E}{E}$ benchmark test cases for a charm jet ($m = 1.2$ GeV, $C_R = \frac{4}{3}$) with fixed $\alpha_s = 0.3$. The path length is $L = 5$ fm; $\hbar c = 0.197$ GeV fm. The density is $\frac{dN}{dy} = 1000$ ($n_f = 0$), giving $T = 0.2403$ GeV, $\mu = 0.4666$ GeV, and $\lambda_g = 1.2465$ fm. For radiative, the q integration limits are taken to be 0.0001 and 50.

where the abbreviated symbols denote

$$K = k_{max}^2 = 2px(1-x) \quad (19)$$

$$Q_\mu^\pm = q^2 \pm \mu^2 \quad (20)$$

$$Q_k^\pm = q^2 \pm k_{max}^2 \quad (21)$$

$$f_\beta = f(\beta, Q_\mu^-, Q_\mu^+) \quad (22)$$

$$f_\mu = f(\mu, Q_k^+, Q_k^-) \quad (23)$$

with $f(x, y, z) = \sqrt{x^4 + 2x^2y + z^2}$.

C. Benchmark Numerical Examples

In this section we record numerical benchmark cases of both the elastic and radiative mean energy loss to illustrate the above formulas. Consider a uniform Bjorken cylinder with density

$$\rho(\tau) = \frac{1}{\pi R^2 \tau} \frac{dN}{dy} \quad (24)$$

We assume $R = 6$ fm. The temperature evolves as

$$T(\tau) = \left(\frac{\pi^2}{1.202} \frac{\rho(\tau)}{9n_f + 16} \right)^{\frac{1}{3}}$$

where n_f is the number of active quark flavors. The effective static approximation simulates the effect of Bjorken expansion by evaluating T at $\tau = L/2$, where L is the jet path length to the the cylinder surface. The gluon density is computed from $\rho_g = \frac{1.202}{\pi^2} \times 16T^3$, and the density of quarks plus antiquarks is $\rho_q = \frac{1.202}{\pi^2} \times 9n_f T^3$. The Debye mass squared is $\mu^2 = 4\pi\alpha_s^2 T^2 (1 + \frac{n_f}{6})$. In Table I the results for $n_f = 0$ are given for a charm jet of energy $10 \leq E \leq 15$.

D. Energy Loss Fluctuation Spectrum

This section illustrates the fluctuation spectra of induced gluon number and the distribution of fluctuating

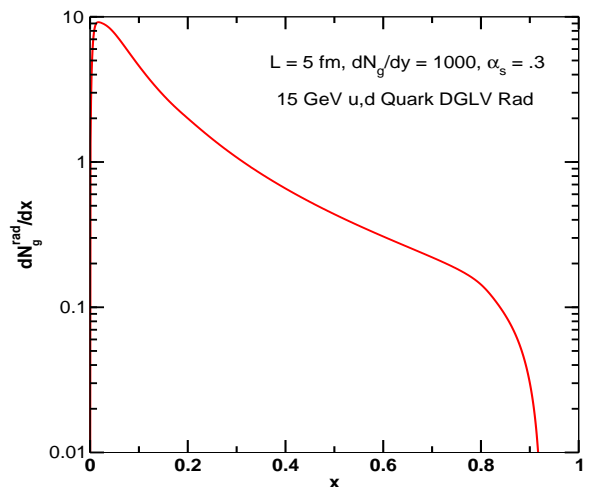


FIG. 9: Example of the induced DGLV radiation gluon number spectrum for a 15 GeV up quark, with path length $L = 5$ fm, $dN_g/dy = 1000$, $\alpha_s = 0.3$, and $A_\perp = 118.7$ fm².

energy loss for a specific case of a 15 GeV up quark jet with path length 5 fm. Fig. 9 shows the first order induced gluon number distribution dN_g/dx for this case. Fig. 10 shows the fractional radiative energy loss distribution taking into account Poisson fluctuations of the gluon number computed as in [4]. The finite probability, $P(n_g = 0) = 0.2377$, of radiating zero gluons contributes a $\delta(\epsilon)$ that is not shown. There is also a finite probability, 0.0213, of complete stopping with $\epsilon > 1$.

The width of the elastic energy fluctuations seen in Fig. 11 is significantly smaller than the radiative width. The narrowing of the convoluted elastic plus radiative distributions significantly reduces the distortion effects due to fluctuations. Because of the steep p_T fall off of the initial unquenched parton spectra, the smaller width of the elastic energy fluctuations considerably amplifies the quenching effect due to collisional energy loss in comparison to the larger but much broader radiative contribution. In terms of an effective renormalization $\langle \epsilon \rangle \rightarrow Z_{eff}(\epsilon)$ as discussed in [4], Z_{eff} is closer to unity than the renormalization $Z_{rad} \sim 0.5$ characteristic of pure radiative energy loss distributions.

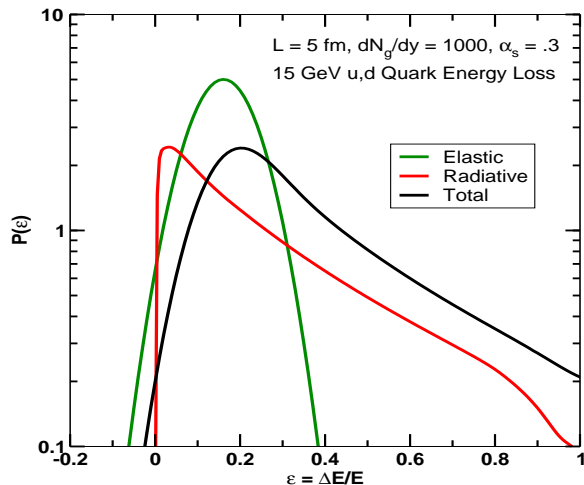


FIG. 10: The distribution of fractional radiative energy loss (or gain), $\epsilon = \Delta E/E$, for the case considered in Fig. 9. The narrow (green) curve corresponds to BT elastic energy loss fluctuations; based on the input from Fig. 9 the lower, broader (red) curve corresponds to inelastic energy loss due to gluon number fluctuations. The part of the radiation spectrum with $\epsilon > 1$ is replaced with $0.0213\delta(1-x)$, and there is a contribution from zero gluon number fluctuations, $0.2377\delta(x)$, not shown. The continuous part of the radiative distribution has integrated norm 0.7374 with mean 0.2026. The top (black) curve corresponds to the convolution of elastic and inelastic energy fraction fluctuations.

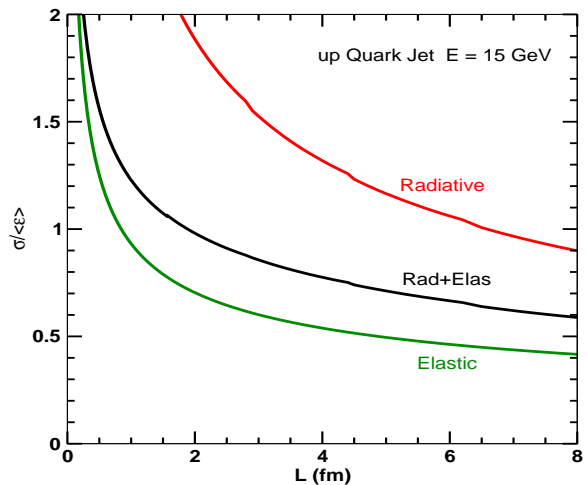


FIG. 11: The ratio of rms width, $\sigma(L)$, to the mean fraction energy loss $\langle \epsilon \rangle$ for radiative, elastic and convolved energy loss distributions is shown as a function of the path length, L , for the Bjorken expanding plasma with $dN_g/dy = 1000$. The case of an up quark jet with $E = 15$ GeV is shown. Notice that the elastic distribution is significantly narrower than the radiative one. This amplifies the effect of elastic energy loss on R_{AA} relative to radiative.

-
- [1] T. Isobe, arXiv:nucl-ex/0510085. M. Shimomura [PHENIX Collaboration], Nucl. Phys. A **774**, 457 (2006) [arXiv:nucl-ex/0510023]. S. S. Adler *et al.* [PHENIX Collaboration], Phys. Rev. Lett. **91**, 072301 (2003) [arXiv:nucl-ex/0304022].
- [2] M. Gyulassy, I. Vitev, X. N. Wang and B. W. Zhang, Quark Gluon Plasma 3, (ed. R.C. Hwa and X.N. Wang, World Scientific, Singapore) pp. 123-191; nucl-th/0302077; A. Kovner and U. Wiedemann, pp. 192-248 op cit. [arXiv:hep-ph/0304151]; P. Jacobs and X. N. Wang, Prog. Part. Nucl. Phys. **54**, 443 (2005) [arXiv:hep-ph/0405125]. X. N. Wang and M. Gyulassy, Phys. Rev. Lett. **68**, 1480 (1992).
- [3] M. Gyulassy, P. Levai and I. Vitev, Nucl. Phys. B **594**, 371 (2001) [arXiv:nucl-th/0006010].
- [4] M. Gyulassy, P. Levai and I. Vitev, Phys. Lett. B **538**, 282 (2002) [arXiv:nucl-th/0112071].
- [5] I. Vitev and M. Gyulassy, Phys. Rev. Lett. **89**, 252301 (2002) [arXiv:hep-ph/0209161];
- [6] S. S. Adler *et al.* [PHENIX Collaboration], Phys. Rev. Lett. **96**, 032301 (2006) [arXiv:nucl-ex/0510047]. Y. Akiba [PHENIX Collaboration], Nucl. Phys. A **774**, 403 (2006) [arXiv:nucl-ex/0510008].
- [7] B. I. Abelev [STAR Collaboration], arXiv:nucl-ex/0607012.
- [8] A. Adare [PHENIX Collaboration], arXiv:hep-ex/0609010.
- [9] J. Bielcik [STAR Collaboration], Nucl. Phys. A **774**, 697 (2006) [arXiv:nucl-ex/0511005]. X. Dong, AIP Conf. Proc. **828**, 24 (2006) [Nucl. Phys. A **774**, 343 (2006)] [arXiv:nucl-ex/0509038].
- [10] A. Adare [PHENIX Collaboration], arXiv:nucl-ex/0611018.
- [11] M. Djordjevic, M. Gyulassy, R. Vogt and S. Wicks, Phys. Lett. B **632**, 81 (2006) [arXiv:nucl-th/0507019].
- [12] BRAHMS, PHOBOS, STAR, and PHENIX Collaborations, BNL-73847-2005; Nucl. Phys. A **757**, 184 (2005), pp. 1, 28, 102, 184.
- [13] BNL Press release, 4/18/05: http://www.bnl.gov/bnl-web/pubaf/pr/PR_display.asp?prID=05-38
- [14] "New Discoveries at RHIC - the current case for the strongly interactive QGP", Proc. RBRC Workshop, May 14-15, 2004, BNL-72391-2004, Nucl. Phys. A **750**, 1, 30, 64, 121 (2005).
- [15] T. Hirano and M. Gyulassy, Nucl. Phys. A **769**, 71 (2006) [arXiv:nucl-th/0506049].
- [16] D. Winter (PHENIX), Quark Matter 2005 talk, <http://www.phenix.bnl.gov/phenix/WWW/publish/winter/QM2005/>
- [17] R. Rapp, V. Greco and H. van Hees, Nucl. Phys. A **774**, 685 (2006) [arXiv:hep-ph/0510050].
- [18] N. Armesto, A. Dainese, C. A. Salgado and U. A. Wiedemann, Phys. Rev. D **71**, 054027 (2005) [arXiv:hep-ph/0501225].
- [19] N. Armesto, M. Cacciari, A. Dainese, C. A. Salgado and U. A. Wiedemann, Phys. Lett. B **637**, 362 (2006)

- [arXiv:hep-ph/0511257].
- [20] R. Baier, Nucl. Phys. A **715**, 209 (2003) [arXiv:hep-ph/0209038].
- [21] M. Cacciari, P. Nason and R. Vogt, Phys. Rev. Lett. **95**, 122001 (2005) [arXiv:hep-ph/0502203].
- [22] M. L. Mangano, P. Nason and G. Ridolfi, Nucl. Phys. B **373**, 295 (1992).
- [23] M. G. Mustafa, Phys. Rev. C **72**, 014905 (2005) [arXiv:hep-ph/0412402]. M. G. Mustafa and M. H. Thoma, Acta Phys. Hung. A **22**, 93 (2005) [arXiv:hep-ph/0311168].
- [24] A. K. Dutt-Mazumder, J. e. Alam, P. Roy and B. Sinha, Phys. Rev. D **71**, 094016 (2005) [arXiv:hep-ph/0411015].
- [25] K. Zapp, G. Ingelman, J. Rathsman and J. Stachel, Phys. Lett. B **637**, 179 (2006) [arXiv:hep-ph/0512300].
- [26] J. D. Bjorken, FERMILAB-PUB-82-059-THY (unpublished).
- [27] M. H. Thoma and M. Gyulassy, Nucl. Phys. B **351**, 491 (1991).
- [28] E. Braaten and M. H. Thoma, Phys. Rev. D **44**, 1298 (1991). Phys. Rev. D **44**, 2625 (1991).
- [29] X. N. Wang, M. Gyulassy and M. Plumer, Phys. Rev. D **51**, 3436 (1995) [arXiv:hep-ph/9408344].
- [30] M. G. Mustafa, D. Pal, D. K. Srivastava and M. Thoma, Phys. Lett. B **428**, 234 (1998) [arXiv:nucl-th/9711059].
- [31] Z. w. Lin, R. Vogt and X. N. Wang, Phys. Rev. C **57**, 899 (1998) [arXiv:nucl-th/9705006].
- [32] D. Molnar and M. Gyulassy, Nucl. Phys. A **697**, 495 (2002) [Erratum-ibid. A **703**, 893 (2002)] [arXiv:nucl-th/0104073].
- [33] G. D. Moore and D. Teaney, Phys. Rev. C **71**, 064904 (2005) [arXiv:hep-ph/0412346].
- [34] Yu. L. Dokshitzer and D. E. Kharzeev Phys. Lett. B **519**, 199 (2001) [arXiv:hep-ph/0106202].
- [35] M. Djordjevic and M. Gyulassy, Nucl. Phys. A **733**, 265 (2004) [arXiv:nucl-th/0310076].
- [36] M. Djordjevic and M. Gyulassy, Phys. Rev. C **68**, 034914 (2003) [arXiv:nucl-th/0305062].
- [37] M. Djordjevic and M. Gyulassy, Phys. Lett. B **560**, 37 (2003) [arXiv:nucl-th/0302069].
- [38] M. Djordjevic, M. Gyulassy and S. Wicks, Phys. Rev. Lett. **94**, 112301 (2005) [arXiv:hep-ph/0410372].
- [39] B. W. Zhang, E. Wang and X. N. Wang, Phys. Rev. Lett. **93**, 072301 (2004) [arXiv:nucl-th/0309040].
- [40] R. Vogt [Hard Probe Collaboration], Int. J. Mod. Phys. E **12**, 211 (2003) [arXiv:hep-ph/0111271].
- [41] J. Pumplin, D. R. Stump, J. Huston, H. L. Lai, P. Nadolsky and W. K. Tung, JHEP **0207**, 012 (2002) [arXiv:hep-ph/0201195]; D. Stump, J. Huston, J. Pumplin, W. K. Tung, H. L. Lai, S. Kuhlmann and J. F. Owens, JHEP **0310**, 046 (2003) [arXiv:hep-ph/0303013].
- [42] H. L. Lai *et al.* [CTEQ Collaboration], Eur. Phys. J. C **12**, 375 (2000) [arXiv:hep-ph/9903282].
- [43] I. Vitev, Phys. Lett. B **562**, 36 (2003) [arXiv:nucl-th/0302002]. ; J. Phys. G **31**, S557 (2005) [arXiv:hep-ph/0409297]; J. W. Qiu, Eur. Phys. J. C **43**, 239 (2005) [arXiv:hep-ph/0507268].
- [44] M. Gyulassy, I. Vitev and X. N. Wang, Phys. Rev. Lett. **86**, 2537 (2001) [arXiv:nucl-th/0012092].
- [45] K. J. Eskola, H. Honkanen, C. A. Salgado and U. A. Wiedemann, Nucl. Phys. A **747**, 511 (2005) [arXiv:hep-ph/0406319].
- [46] B. Hahn, D. G. Ravenhall and R. Hofstadter, Phys. Rev. **101**, 1131 (1956).
- [47] W. Horowitz, S. Wicks, M. Gyulassy, in preparation.
- [48] S. Peigne, P. B. Gossiaux and T. Gousset, JHEP **0604**, 011 (2006) [arXiv:hep-ph/0509185].
- [49] A. Adil, M. Gyulassy, W. A. Horowitz and S. Wicks, arXiv:nucl-th/0606010.
- [50] M. Djordjevic, arXiv:nucl-th/0603066.
- [51] X. N. Wang, arXiv:nucl-th/0604040.
- [52] A. Peshier, arXiv:hep-ph/0605294.